East Tennessee State University
Digital Commons @ East Tennessee State University

ETSU Faculty Works | Faculty Works

1-1-2009

Modeling Forbidden Line Emission Profiles from Colliding Wind Binaries.

Richard Ignace
East Tennessee State University

R. Bessey
Georgia Tech

C. Price

Follow this and additional works at: https://dc.etsu.edu/etsu-works

 Part of the Stars, Interstellar Medium and the Galaxy Commons

Citation Information

Ignace, Richard; Bessey, R.; and Price, C.. 2009. Modeling Forbidden Line Emission Profiles from Colliding Wind Binaries.. *Monthly Notices of the Royal Astronomical Society*. Vol.395(2). https://doi.org/0.1111/j.1365-2966.2009.14586.x ISSN: 0035-8711

This Article is brought to you for free and open access by the Faculty Works at Digital Commons @ East Tennessee State University. It has been accepted for inclusion in ETSU Faculty Works by an authorized administrator of Digital Commons @ East Tennessee State University. For more information, please contact digilib@etsu.edu.

Modeling Forbidden Line Emission Profiles from Colliding Wind Binaries.

Copyright Statement

This article has been accepted for publication in Monthly Notices of the Royal Astronomical Society © 2009 The Authors. Published by Oxford University Press on behalf of the Royal Astronomical Society. All rights reserved. doi:10.1111/j.1365-2966.2009.14586.x

This article is available at Digital Commons @ East Tennessee State University: https://dc.etsu.edu/etsu-works/6266

Mon. Not. R. Astron. Soc. **395,** 962–972 (2009) doi:10.1111/j.1365-2966.2009.14586.x

Modelling forbidden line emission profiles from colliding wind binaries

R. Ignace,★ R. Bessey† and C. S. Price

Department of Physics and Astronomy, East Tennessee State University, Box 70652, Johnson City, TN 37614, USA

Accepted 2009 February 2. Received 2009 January 19; in original form 2008 December 9

ABSTRACT

This paper presents calculations for forbidden emission-line profile shapes arising from colliding wind binaries. The main application is for systems involving a Wolf–Rayet (WR) star and an OB star companion. The WR wind is assumed to dominate the forbidden line emission. The colliding wind interaction is treated as an Archimedean spiral with an inner boundary. Under the assumptions of the model, the major findings are as follows. (i) The redistribution of the WR wind as a result of the wind collision is not flux conservative but typically produces an excess of line emission; however, this excess is modest at around the 10 per cent level. (ii) Deviations from a flat-topped profile shape for a spherical wind are greatest for viewing inclinations that are more nearly face-on to the orbital plane. At intermediate viewing inclinations, profiles display only mild deviations from a flat-topped shape. (iii) The profile shape can be used to constrain the colliding wind bow shock opening angle. (iv) Structure in the line profile tends to be suppressed in binaries of shorter periods. (v) Obtaining data for multiple forbidden lines is important since different lines probe different characteristic radial scales. Our models are discussed in relation to *Infrared Space Observatory* data for WR 147 and γ Vel (WR 11). The lines for WR 147 are probably not accurate enough to draw firm conclusions. For γ Vel, individual line morphologies are broadly reproducible but not simultaneously so for the claimed wind and orbital parameters. Overall, the effort demonstrates how lines that are sensitive to the large-scale wind can help to deduce binary system properties and provide new tests of numerical simulations.

Key words: binaries: close – stars: early-type – stars: mass-loss – stars: winds, outflows – stars: Wolf–Rayet.

1 INTRODUCTION

Massive star colliding wind systems continue to be an area of intense study. The colliding wind interaction region (CWIR) is intrinsically interesting as a problem of hydrodynamic flow (Girard & Willson 1987; Shore & Brown 1988; Stevens, Blondin & Pollock 1992; Usov 1992; Canto, Raga & Wilkin 1996; Gayley, Owocki & Cranmer 1997). The CWIRs lead to a number of interesting observable effects as well, such as the X-ray emissions (e.g. Stevens et al. 1996; Maeda et al. 1999; Zhekov & Skinner 2000; Pittard et al. 2002; Henley, Stevens & Pittard 2003), ultraviolet (UV) and infrared (IR) emission-line profile effects (e.g. Stevens 1993; Lührs 1997; Stevens & Howarth 1999; Hill et al. 2000; Hill, Moffat & St-Louis 2002), dust emission (e.g. Monnier, Tuthill & Danchi 1999; Tuthill, Monnier & Danchi 1999; Tuthill et al. 2006, 2008) and polarization (e.g. Brown, McLean & Emslie 1978; Drissen et al. 1986; Villar-Sbaffi, Moffat & St-Louis 2003; Villar-Sbaffi et al. 2005, 2006). Of chief interest between relating the observables to the hydrodynamical predictions are the determinations of the mass-loss rates for the two stars, their orbital properties and the opening angle of the colliding wind bow shock. Obtaining the orbital solution implies deriving the masses of the two stars, which is important for understanding massive star evolution. As is typical with unresolved binary systems, the viewing inclination i creates a challenge to obtaining the full orbital solution and stellar masses.

In the study of CWIRs of massive binaries, the interpretation of optically thin lines remains prominent, such as X-ray lines that encode information about opening angle and viewing inclination. One area that has been largely ignored is the influence of the CWIR on the *shape* of forbidden emission-line profiles, especially those in the IR. The *Infrared Space Observatory* ('*ISO*') and the *Spitzer Space Telescope* ('*Spitzer*') have provided a large quantity of high-quality IR spectra for massive stars. Especially in the case of the evolved Wolf–Rayet (WR) stars, the IR spectra are rich in emission lines and, in particular, forbidden lines. These forbidden lines have been useful for deriving or constraining gaseous abundances that are relevant for testing models of massive star evolution (e.g. Barlow, Roche & Aitken 1988; Willis et al. 1997; Dessart et al. 2000; Morris et al. 2000; Morris, Crowther & Houck 2004; Smith & Houck 2005; Ignace et al. 2007).

An interesting property of these forbidden lines is that they form at large radius in the wind of a WR star. Consequently, the line formation occurs well beyond the wind acceleration thus sampling

★E-mail: ignace@etsu.edu
†Currently at Georgia Tech.

© 2009 The Authors. Journal compilation © 2009 RAS

Downloaded from http://mnras.oxfordjournals.org/ at James H. Quillen College of Medicine Library on October 5, 2015

the flow at the wind terminal speed v_∞. Being optically thin, these forbidden lines should be flat-topped in shape, and so they are excellent for measuring v_∞ values (Barlow et al. 1988).

But the flat-topped profile morphology only holds if the wind is spherically symmetric. If a WR star is part of a binary, then even if the WR wind is intrinsically spherically symmetric, the CWIR ensures that it will not remain so. Equally interesting is the fact that forbidden lines can form over tens of thousands of WR stellar radii (e.g. Ignace et al. 2001), corresponding to scales of several au and comparable to binary separations in massive star binaries. As a result, forbidden emission profiles should not be flat-topped, in general, in these systems, and their deviation from flat-top – like the case for other CWIR emission-line diagnostics – can be used to constrain the properties of the CWIR geometry.

In this paper, we calculate a range of forbidden line profile shapes as a function of wind and orbit parameters. Section 2 presents a brief overview of forbidden line formation, a derivation of emission profiles in a spherical wind, and then in a colliding wind system. Then Section 3, describes applications to two systems: WR 147 and γ Vel. Concluding remarks are given in Section 4.

2 FORBIDDEN LINE FORMATION IN WINDS

Our presentation of the theory of forbidden line emission generally follows Osterbrock (1989) regarding the atomic physics, Barlow et al. (1988) for application to winds and Ignace & Brimeyer (2006) for notation. The following sections describe (i) the two-level approximation for forbidden lines, (ii) the solution for the forbidden line emission in a spherical wind, (iii) the adopted model used to describe a CWIR between a WR star and an OB star and (iv) adjustments to the forbidden line profile calculation arising from the CWIR.

2.1 The atomic physics

For simplicity, the two-level atom approximation is adopted for a fine-structure transition of an ion species. The lower level will be '1' and the upper level '2'. It is common to introduce a critical density n_c that signifies the transition from the higher density medium where de-excitations are dominated by collisions versus the lower density zone where spontaneous decay dominates. Since excitation is assumed to derive from collisions *only*, the emissivity transitions from a function that is linear in density in the collisional regime to one that is quadratic in density in the decay regime. The critical density is defined as

$$n_c = \frac{A_{21}}{q_{21}}, \tag{1}$$

where A_{21} (s^{-1}) is the Einstein A-value for the transition and q_{21} is the downward volume collisional de-excitation rate ($cm^3\ s^{-1}$). The volume emissivity j (erg s^{-1} cm^{-3} sr^{-1}) is

$$j = \frac{1}{4\pi}\, h\, \nu_{21}\, A_{21}\, n_2. \tag{2}$$

In the two level atom, the entire density of elemental species E in ion stage i is given by $n_{E,i} = n_1 + n_2$. One can derive the ratio n_2/n_1 from equilibrium conditions and use that to solve for the population of the upper level (Barlow et al. 1988):

$$n_2 = \frac{n_{i,E}\, n_e\, q_{12}}{n_e\, q_{12} + n_e\, q_{21} + A_{21}}, \tag{3}$$

where

$$\varpi \equiv \frac{q_{21}}{q_{12}} = \frac{g_1}{g_2}\, e^{\beta}, \tag{4}$$

with

$$\beta = h\nu_{21}/kT_e, \tag{5}$$

for ν_{21} the frequency of the line transition, T_e the electron temperature and g_J the statistical weight of the level, with $g_J = 2J + 1$. The downward collisional volume rate is given by

$$q_{21} = \frac{8.629 \times 10^{-6}}{T_e^{1/2}}\, \frac{\omega_{12}}{g_2}, \tag{6}$$

where ω_{12} is the collision strength. A summary of line transition data and critical densities is given in Table 1.

Forbidden emission lines in stellar winds are optically thin. The above relations are typically combined with the intent of integrating the emissivity over the wind and solving for the ionic abundance, derivable from observed forbidden emission lines and used to constrain gas abundances in evolved stars to test massive star evolution models. The primary goal of our paper is quite different. We seek to derive line profile *shapes* to determine to what extent those shapes may be used to deduce the properties of binary orbits and stellar winds in colliding wind systems. To do so, we first review the solution for a spherical wind.

2.2 Spherical winds

It is useful to review briefly the line emission for a forbidden line from a spherically symmetric wind, both to establish notation and as a reference to use with the non-spherical case. For a spherical wind with mass-loss rate $\dot{M}$ and radial speed $v(r)$ for radius r, the mass density is

$$\rho_{sph} = \frac{\dot{M}}{4\pi\, r^2\, v(r)}. \tag{7}$$

Table 1. Forbidden line data[a].

Ion	Transition	g_1	g_2	λ (μm)	β^b	ϖ	A_{21} (10^{-3}) s^{-1}	Ω^b	n_c (10^4) cm^{-3}
Ca IV	$^2P_{1/2} \rightarrow {}^2P_{3/2}$	4	2	3.2	0.45	3.14	545	1.06	1200
Ne II	$^2P_{1/2} \rightarrow {}^2P_{3/2}$	4	2	12.8	0.113	2.24	8.55	0.30	65.0
Ne III	$^3P_1 \rightarrow {}^3P_2$	5	3	15.6	0.092	1.83	5.97	1.65	12.6
S IV	$^2P_{3/2} \rightarrow {}^2P_{1/2}$	2	4	10.5	0.137	0.57	7.73	6.42	5.6
O IV	$^4P_{5/2} \rightarrow {}^4P_{1/2}$	2	6	32.6	0.044	0.35	0.518	0.69	5.2
Ne V	$^3P_2 \rightarrow {}^3P_1$	3	5	14.3	0.101	0.66	4.59	5.82	4.6
S III	$^3P_2 \rightarrow {}^3P_1$	3	5	18.7	0.077	0.65	2.07	5.81	2.1
Si III	$^3P_2 \rightarrow {}^3P_1$	3	5	38.2	0.038	0.62	0.242	10.4	0.13

[a]Atomic data taken from Pradhan & Peng (1995).
[b]Evaluated for $T_e = 10^4$ K.

© 2009 The Authors. Journal compilation © 2009 RAS, MNRAS **395,** 962–972

Downloaded from http://mnras.oxfordjournals.org/ at James H. Quillen College of Medicine Library on October 5, 2015

The electron number density is $n_e = \rho_{sph}/\mu_e m_H$, for μ_e the mean molecular weight per free electron.

The region of line formation is set roughly by the radius at which $n_e = n_c$. For hot stars $\dot{M} \sim 10^{-10}\,M_\odot\,yr^{-1}$ and larger, with $v_\infty \sim 1000\,km\,s^{-1}$ or more for OB stars (e.g. Lamers & Cassinelli 1999). To estimate the radius of line formation, we introduce an electron number density scalefactor that depends on these basic wind parameters:

$$n_{0,e} = \frac{\dot{M}}{4\pi R_*^2\, v_\infty\, \mu_e\, m_H}. \tag{8}$$

Then, the critical radius becomes

$$\frac{r_c}{R_*} = \sqrt{\frac{n_{0,e}}{n_c}}. \tag{9}$$

With $n_{0,e}$ of the order of $10^{13}\,cm^{-3}$ for a WR star, and n_c about $10^5\,cm^{-3}$, forbidden line emission forms in the far wind, around $10^4 R_*$.

To determine the emission-line shape, we combine equations (2) and (3) to obtain the emissivity:

$$j = j_0\,\frac{D_c\, n_e/n_{0,e}}{1 + \varpi + \varpi\, D_c\, n_e/n_{0,e}}, \tag{10}$$

where j_0 is a constant that depends on the line of interest, $D_c \geq 1$ is the 'clumping factor' that introduces a dependence on the wind clumping (following Dessart et al. 2000). Note that Ignace & Brimeyer (2006) did not account for clumping in their expressions.

The total luminosity of the optically thin line emission is given by a volume integration involving the emissivity:

$$L_l = 4\pi \int j(r)\, D_c^{-1}\, r^2\, dr\, d\cos\vartheta\, d\varphi. \tag{11}$$

where (r, ϑ, φ) are spherical coordinates in the star system, and the inverse of the clumping factor is the volume filling factor. Substituting for a normalized radius $x = r/R_*$ and inserting the emissivity function above, one has

$$L_l = \frac{L_0}{4\pi} \int \frac{dx\, d\cos\vartheta\, d\varphi}{1 + \varpi + \varpi\, D_c^{-1}\,(x/x_c)^2}, \tag{12}$$

where $L_0 = 16\pi^2 j_0 R_*^3$, and the line is assumed to form predominantly over the constant velocity flow where $\rho \propto r^{-2}$ since $x_c \gg 1$ (cf. fig. 1 of Ignace & Brimeyer 2006).

The angular quantities integrate to 4π, and the radial integral is of a standard form. Given that $x_c \gg 1$, the total line luminosity becomes

$$L_l \approx L_0\,\frac{\pi/2}{\sqrt{(1+\varpi)\,\varpi}}\,\sqrt{D_c}\,x_c. \tag{13}$$

Note that a constant clumping factor appears as a square root coefficient to the critical radius, and so the product acts essentially as a 'transformed' critical radius. Also note that the scale constant L_0 depends on the mass-loss rate. The assumption is that equation (13) holds if $\dot{M}$ is *already* a clumping-corrected value.

This, of course, is the total volume-integrated emission. More relevant to our study is the emission profile shape. Optically thin lines that form in a constant expansion and spherically symmetric wind produce flat-topped emission profiles. The isovelocity zones are given by

$$v_z = -v_\infty\,\cos\theta = -v_\infty\,\mu, \tag{14}$$

where θ is the polar angle from the observer axis z. With v_z fixed, the isovelocity zones are cones. Introducing $w_z = v_z/v_\infty$, and noting that $dw_z = -d\mu$, the profile shape $dL_l/dv_z = \lambda^{-1} L_\nu$ becomes

$$\frac{dL_l}{dv_z}(w_z) = \frac{1}{2}\,\frac{L_l}{v_\infty}. \tag{15}$$

In the consideration of line shapes from colliding wind systems, the above constructions will continue to prove useful.

2.3 Colliding wind binaries

Ignace & Brimeyer (2006) explored the effects of axisymmetric density distributions for forbidden lines shapes from single star winds. In that study the key parameters that determined deviations from flat-toped morphologies were the viewing inclination, the latitudinal density description (whether bipolar or disc-like flow) and the ionization balance. The colliding wind systems allow for considerably more influences, in part because the system is completely non-axisymmetric and also because there are really two sets of parameters to consider – those of the orbit and those of the stellar winds.

In order to explore the range of line shapes and their relevance for observations, some approximations will be adopted. We consider WR+OB systems such that it is the WR wind that dominates the emission of the forbidden line. This is reasonable because the mass loss is much higher and the abundances are non-solar for the WR component. For example, [Ne III] at 15.56 μm is typically prominent across WR subtypes (Ignace et al. 2007), and neon can be enhanced above solar by factors of a few or much more in a WC wind. As a result, one major assumption of our study is that the confined wind of the OB companion as dominated by the more massive WR wind will have zero emissivity.

As noted before, the forbidden lines form at large radii (i.e. compared to the stellar sizes, but not necessarily larger than the orbit size). We will assume that the WR wind is in constant expansion for evaluating the line profile shape.

For the binary, we choose to work in a frame centred on the WR star (see Fig. 1). The OB companion is taken to follow an elliptical orbit of semimajor axis a and eccentricity e. The observer is located on the z axis, and the normal to the orbit plane is defined to be z_*. The viewing inclination is given by $\cos i = \hat{z}\hat{z_*}$.

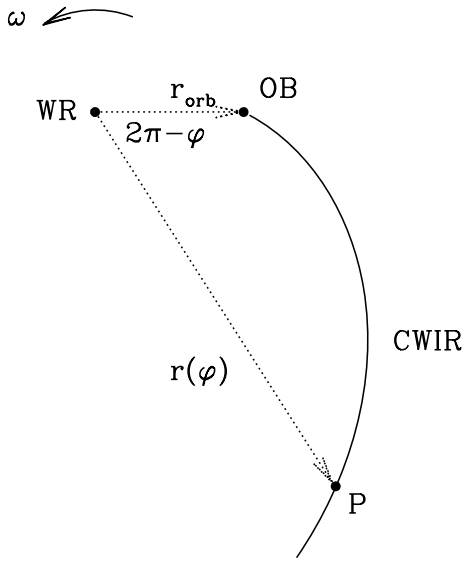

Figure 1. Schematic of the spiral CWIR in the binary orbital plane. The WR star is at left and the OB companion at right. In this 'snapshot', the binary separation is r_{orb}. The orbital motion is counterclockwise as signified by the angular speed ω, and so the spiral CWIR winds out in a clockwise fashion. A point along the CWIR P is indicated as having polar coordinates r and $2\pi - \varphi$.

Downloaded from http://mnras.oxfordjournals.org/ at James H. Quillen College of Medicine Library on October 5, 2015

The WR coordinate system is described by spherical coordinates (r, ϑ, φ) and Cartesian coordinates (x_*, y_*, z_*). The observer frame also centred on the WR star has coordinates (r, θ, α) and (x, y, z). The x–z and x_*–z_* planes are taken as coincident. Azimuthal angles are measured counterclockwise in standard fashion from the x and x_* axes. The reference point for the orbit is the periastron location φ_p. At any given epoch, the OB star will be located at azimuth φ_s, which we take to be the orbital phase.

The CWIR will be described in a largely asymptotic form. We consider the interaction region to have two primary zones: a shocked layer for the OB star wind and a shocked layer for the WR wind. The interface is taken to describe the confinement of the OB wind. Since we ignore any line emission from the OB wind, the trace of that interface and its interior is treated as an emission 'cavity'. Line emission then arises from two sectors only. The first is the shocked WR wind. The second is an approximately spherical WR wind that exists outside the shock layer.

The asymptotic shape of the CWIR is that of a spiral, motivated by observations of 'pinwheel' nebula from dust and radio emission in several WR binaries (e.g. Monnier et al. 2002). If the OB companion is at azimuth φ_s and orbiting counterclockwise, then the interaction region spirals outward in a clockwise direction, and vice versa. We assume that the bow shock at the OB star has circular cross-section. The 'memory' of that interaction is moving radially outwards at a constant speed. The intersection of the spiral interaction region with a spherical shell centred on the WR star is assumed to maintain a constant solid angle of circular cross-section.

The following relations describe the CWIR as related to the binary orbit. The OB star is located at a radius $r_{\rm orb}$ in the orbital plane as given by

$$r_{\rm orb} = a\,\frac{1-e^2}{1+e\cos(\varphi-\varphi_{\rm p})}. \tag{16}$$

At this distance, the interface between the WR and OB star winds is taken to have a half-opening angle β. The shocked layer of the WR wind is taken to have a half-opening angle β'. Thus, the intersection of a spherical shell with the compressed WR wind layer appears as an annulus of angular width $\Delta\beta = \beta' - \beta$. The characteristic lateral lengths l and l' associated with these angles are:

$$l = r_{\rm orb}\,\tan\beta, \tag{17}$$

and

$$l' = r_{\rm orb}\,\tan\beta'. \tag{18}$$

Assuming the shock is strong, the immediate post-shock density will be four times that in the normal spherical WR wind component. Assuming an adiabatic shock layer with constant post-shock density, then the annular cross-section of the shocked layer has one-quarter the solid angle of the confined OB wind, leading to the follow relation that we adopt for our models:

$$\cos\beta' = \frac{5\cos\beta - 1}{4}. \tag{19}$$

Note that we treat β largely as a free parameter in our models to explore profile shape effects. In fact, its value should be related to the ratio of wind momenta for the WR and OB star winds. We define

$$\epsilon = \frac{(\dot{M}v_\infty)_{\rm OB}}{(\dot{M}v_\infty)_{\rm WR}}. \tag{20}$$

Then, the stagnation point between the two stars will be located at a radius r_0 from the WR star as given by (e.g. Shore & Brown 1988)

$$r_0 = \frac{r_{\rm orb}}{1+\sqrt{\epsilon}}. \tag{21}$$

Recently, Gayley, Parsons & Owocki (in preparation) have considered the opening angle associated with a purely adiabatic shock, which is the case adopted for our work, in contrast to a radiative shock (see Canto et al. 1996; Antokhin, Owocki & Brown 2004). Gayley et al. (in preparation) derive the following transcendental relation for the shock cone opening angle:

$$\cos\beta = \frac{1+\epsilon^2-2\epsilon}{1-\epsilon^2}. \tag{22}$$

This expression will be used in our application to WR 147 later in this paper.

Interior to the orbit, the WR wind is assumed spherical. The bow shock region in the vicinity of the OB star will be dominated by hot, X-ray emitting gas (e.g. Parkin & Pittard 2008). Consequently, the requisite ions for contributing to the forbidden lines simply would not exist there. As a result, we model the bow shock zone OB star with cut offs. We assume that the confined OB wind (hereafter referred to as the 'cavity') and the compressed WR wind (hereafter simply the 'compressed layer') extend to the stagnation point r_0 between the two stars and are too hot to produce forbidden line emission for the ions of interest. We further assume that the gas remains hot some distance downstream of $r_{\rm orb}$. We adopt $8r_0$ for this distance, using Cassinelli et al. (2008) for adiabatic shocked wind flow around a blunt object as a crude guide. As long as $a \ll r_c$ or $a \gg r_c$, the details of the bow shock region will not greatly impact the forbidden line profile shape. It is more relevant when $a \sim r_c$, in which case our results can only be taken as illustrative.

It remains then only to trace the centre of the cavity with distance and azimuth in the orbital plane to completely define the spiral interaction region through the WR wind. A cross-section of the spiral pattern is basically a 'shadow' of the wind collision that advances through the WR wind at constant radial expansion. We simply need an expression for the star's location around the orbit with phase to determine an equation of motion for this 'shadow'. Such a relation is derivable from Kepler's laws.

At any given phase, the cross-section centre advances radially according to

$$\dot{r} = v_\infty. \tag{23}$$

Conservation of angular momentum $\mathcal{L}$ provides a relation for the star location:

$$\dot{\varphi_*} = \frac{\mathcal{L}}{r_{\rm orb}^2}, \tag{24}$$

with the specific angular momentum given by

$$\mathcal{L} = \sqrt{GMa\,(1-e^2)} \tag{25}$$

for M the summed mass of the two stars. Defining an angular velocity $\omega = 2\pi/P$ for period P, using Kepler's third law, and combining the three preceding equations, a differential equation for the cross-section centre can be derived:

$$\frac{{\rm d}\varphi_*}{{\rm d}r} = -\frac{a^2/r_{\rm orb}^2}{r_{\rm w}}\sqrt{1-e^2}, \tag{26}$$

where a convenient scaling parameter we call the 'wrapping length' $r_{\rm w}$ is introduced:

$$r_{\rm w} = v_\infty/\omega. \tag{27}$$

Downloaded from http://mnras.oxfordjournals.org/ at James H. Quillen College of Medicine Library on October 5, 2015

The wrapping length is related to the pitch angle of the spiral shape. Since r_c is a scale for the emission of the line, it is natural to characterize models by the ratio $2\pi r_w/r_c = P/t_c$, where $t_c = r_c/v_\infty$ indicating the number of wrappings per critical radius crossing time. If the wind flow time across the critical radius is much longer than P, the spiral will have many circuits over that scale; but if the orbital period is long, the spiral is essentially a cone over the span of a critical radius.

2.4 Conical interaction regions

Before tackling the case of general orbits, it is instructive to consider the extremely long period binaries for which the bow shock geometry is asymptotically conical in shape, having no spiral curvature. We will refer to this limit as the 'conical' (or 'linear') bow shock.

In the approximation of negligible wrapping of the spiral, the cavity and compressed layer are cones centred on the line of centres for the two stars. The isovelocity zones are also cones. An important point is that we assume the flow in the compressed layer is radial and has the same speed as the WR terminal speed. This is a reasonable approximation for an adiabatic shock and a strong WR wind (see Tuthill et al. 2008). These isovelocity cones are centred on the observer's line-of-sight, and so are inclined to that of the CWIR. What is interesting is that the intersection of the interaction region with the isovelocity cones is a fixed pattern with radius.

Consider a spherical shell. The cross-sections of the isovelocity zones are rings. The cross-section of the interaction region is a ring also which, without loss of generality, is assumed to lie in the x–z plane. It is straightforward to find the crossing points between the two rings in terms of the azimuthal angle α_0 for the observer (see Fig. 2). If the cavity centre is at $\theta_c = 90^\circ - i$, the implicit solution for α_0 is

$$\cos\beta = \cos\theta_c \cos\theta + \sin\theta_c \sin\theta \cos\alpha_0, \tag{28}$$

$$= w_z\, w_c + \cos\alpha_0 \sqrt{(1 - w_z^2)(1 - w_c^2)}, \tag{29}$$

w_z is the observed normalized velocity shift in the line and w_c is the value for the isovelocity zone for the cavity axis. The same relation can be used for β' and α_0' to determine the crossing points between an isovelocity ring on the shell and the circular boundary of the compression layer. The key is that α_0 and α_0' are constants with radius.

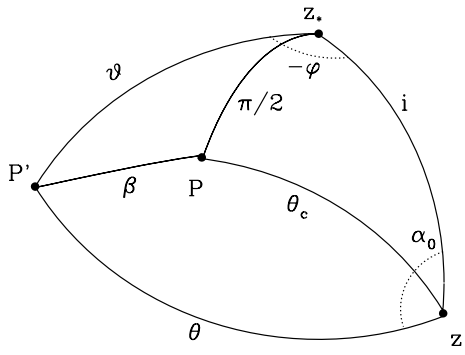

Figure 2. Geometry related to the conical interaction region and the evaluation of equation (28). The z point is towards the observer and the z_* is the binary orbital axis. Point P signifies the axis of the conical CWIR, and point P' is located on the shock contact discontinuity. A similar set of spherical triangles would apply for a point on the boundary of the compressed layer at angles β' and θ'.

There are several special cases that are notable. If viewed pole-on, intersections only occur for $\theta > 90^\circ - \beta'$ and $\theta < 90^\circ + \beta'$. When viewed edge-on, the axis of the interaction region coincides with the z-axis, in which case there is no emission for $\theta < \beta$, and emission from the compressed layer is exclusively from $\beta < \theta < \beta'$.

For emission from the compression region, the density is enhanced by a constant factor of 4 in our treatment. In terms of the emission per unit solid angle, $dL_v/d\Omega$, the integration along a hypothetical radial that lies entirely within the compression layer will be eight times greater than for one in a purely spherical wind. Of course, the compression layer has a solid angle extent that is one-fourth that of the cavity. In effect, the wind collision redistributes mass in a sector of the WR flow, and there is a net gain in line emission above what that sector would have produced if it were undisturbed. The wind collision leads in essence to a globally structured clump. The important point is that one should not expect CWIRs to conserve flux in the forbidden line as compared to a spherical wind.

Also, the CWIR does not extend down to the photosphere of the WR star, but is significantly offset in radius, as determined by the location of the stagnation point on the line of centres between the two stars and the width of the compressed WR wind. This means there is a minimum radius to the CWIR, interior to which a spherical WR wind makes a simple flat-toped contribution to the line profile.

Example profiles for the conical bow shock approximation are shown in Fig. 3 for different binary separations relative to the critical radius a/r_c, cavity opening angles β and viewing inclinations i. Model parameters for the different panels are provided in Table 2. The principle conclusions are that: (i) only a pole-on view to the orbit produces a symmetric profile, with a double-horned appearance, (ii) an edge-on view produces one that is maximally lopsided and (iii) generally an asymmetric double-horned profile shape results whose appearance relates to the viewing perspective and orbital

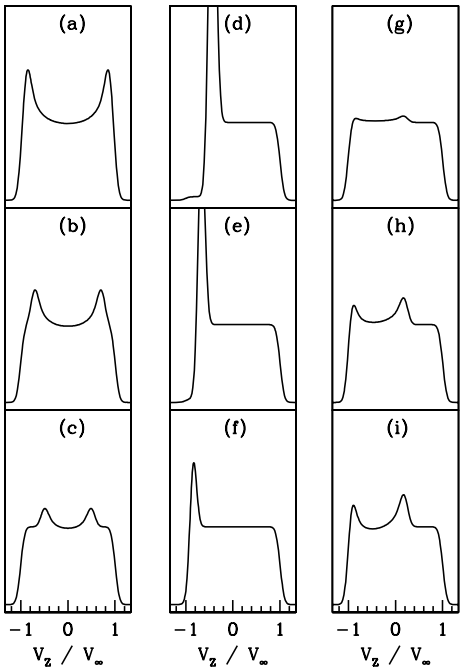

Figure 3. Model line profiles in the 'conical bow shock' (i.e. $r_w \gg r_c$). Each profile is normalized to have unit area, and the horizontal axis is normalized velocity shift. Table 2 details the model parameters for each panel.

Downloaded from http://mnras.oxfordjournals.org/ at James H. Quillen College of Medicine Library on October 5, 2015

Table 2. Model runs for Fig. 3.

Panel	a/r_c	β (°)	i (°)
(a)	0.1	60	0
(b)	0.1	45	0
(c)	0.1	30	0
(d)	0.1	60	90
(e)	0.1	45	90
(f)	0.1	30	90
(g)	10	40	30
(h)	1	40	30
(i)	0.01	40	30

parameters. Note that these profiles have been Gaussian smoothed to simulate limited spectral resolution. Given that typical WR winds have $v_\infty \approx 1000$–$3000\,\mathrm{km\,s^{-1}}$, smoothing with a Gaussian of half width at half maximum (HWHM) $\delta v/v_\infty = 0.1$ was adopted to match roughly the resolution of *ISO*'s SWS06 instrument (de Graauw et al. 1996).

Finally, all of the examples in Fig. 3 have *excess* emission relative to a purely spherical wind by factors of 10–20 per cent. It happens that the total line flux as a function of the opening angle and binary separation is derivable analytically. There are four basic zones. As previously noted for radii $r < r_{\rm orb}$, the WR wind is spherical and contributes a flat-toped contribution to the profile. In the cavity sector, there is no contribution. Then, there is the spherical zone and the compressed layer for $r \geq r_{\rm orb}$. Accounting for these zones, the solution for the line luminosity, relative to a pure spherical wind, is denoted by Λ and given by

$$\Lambda = 1 + \frac{2}{\pi}(1-\cos\beta)\left[\tan^{-1}\left(\frac{2\sigma\, u_0}{u_c}\right) - \frac{5}{8}\tan^{-1}\left(\frac{\sigma\, u_0}{u_c}\right)\right], \quad (30)$$

where

$$\sigma = \sqrt{\frac{D_{\rm cl}\,\varpi}{1+\varpi}}. \quad (31)$$

In the limit that $\beta = 0$, equation (30) reduces to unity, as it must because there is no CWIR. For two identical winds, the opening angle is $\beta = 90°$, and the maximum line flux for a given value of $\sigma u_0/u_c = \sigma r_c/r_0$ becomes

$$\Lambda = 1 - \frac{5}{4\pi}\tan^{-1}\left(\frac{\sigma\, u_0}{u_c}\right) + \frac{2}{\pi}\tan^{-1}\left(\frac{2\sigma\, u_0}{u_c}\right). \quad (32)$$

If the binary orbit is exceedingly large, $\Lambda = 1$ is again recovered because the CWIR is displaced to a location of irrelevance with $r_{\rm orb} \gg r_c$. On the other hand, if $r_c \gg r_{\rm orb}$, all the arctangent factors reduce to $\pi/2$, thus

$$\Lambda = \frac{11 - 3\cos\beta}{8}. \quad (33)$$

Formally, this has a maximum of 1.75. Fig. 4 shows $(\Lambda - 1)$ as a percentage excess of line emission above the spherical value as a function of $\sigma\, r_c/r_0$. The different curves are for different β values, from 0° to 90° in 10° increments, with the excess being greater for larger β. The location of maximum *percentage* excess can be derived from equation (30) and occurs at $\sigma r_c/r_0 = \sqrt{11}/2$ for all β.

These curves are accurate only within the assumptions for the adopted geometry. A different set of curves would result, for example, if the relation between β' and β were different. Also, for ease of calculation, the bow shock exists for $r \geq r_{\rm rob}$ and not at all for interior radii, which is incorrect because this neglects the shape of the head of the bow shock. The exercise does serve to demonstrate that (i) colliding wind effects will generally not conserve line flux, (ii) line flux excesses at the level of ∼10 per cent can be expected, (iii) the excess will depend on the clumping factor in the large-scale wind and (iv) elemental abundance determinations for WR winds from forbidden lines formed in colliding wind systems are not dramatically biased by the CWIR. However, it may be that changes in ionization between the nominal spherical wind and the compressed layer could have a larger systematic influence that would need to be investigated more carefully in detailed simulations. We attempt to include such affects in our consideration of applications to WR 147 and γ Vel in Section 3.

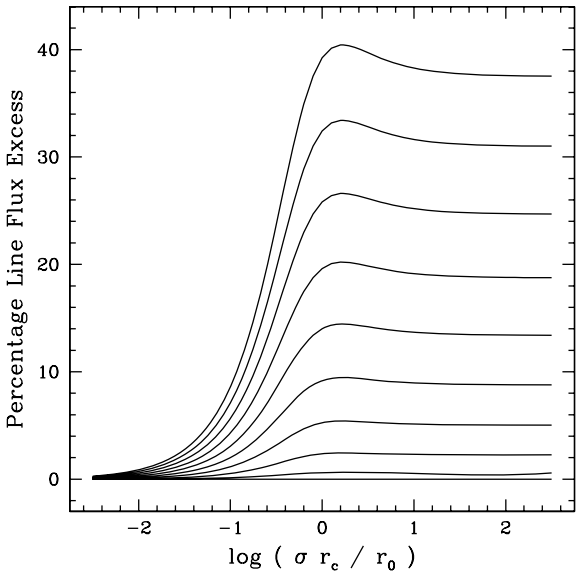

Figure 4. A plot of the integrated *excess* line flux for a colliding wind system as compared to a single spherical wind. This is plotted against the ratio of the critical radius associated with the line relative to the separation of the WR star and OB companion. An additional dimensionless multiplicative factor, σ, accounts for the wind clumping and atomic constants for the transition (see equation 31).

2.5 Spiral interaction regions

For spiral-shaped interaction regions when binary orbital effects are important, issues that influence the profile shape are similar as for the conical-shaped regions of the last section. However, there are a few more important factors to bear in mind. The spiral is still symmetric about the orbital plane. That means the line profile should be symmetric about zero velocity for a pole-on inclination of the system. However, when edge-on the spiral shape now allows the interaction region to transit (eventually) *every* isovelocity zone, thereby tending to dilute the influence of non-sphericity in the profile shape. Another important factor is that the direction of orbital revolution with respect to the observer will be relevant.

One expects the following trends to hold.

(i) Larger opening angles lead to profile structure over a greater range of observed velocity shifts.

(ii) Flat-toped segments seen towards the line wings place a limit on $i - \beta'$.

© 2009 The Authors. Journal compilation © 2009 RAS, MNRAS **395,** 962–972

Downloaded from http://mnras.oxfordjournals.org/ at James H. Quillen College of Medicine Library on October 5, 2015

(iii) The total line luminosity derivation of equation (30) for the conical interaction regions remains relevant for the spiral case. With the assumption of constant solid angles, the proportions of the cavity and compressed layer to a spherical shell are constant with radius. This means that a spiral interaction region is simply a conical one with radius-dependent phase lags. However, those curves require a correction for the extension of the emission cavity down to the stagnation point in regimes where that portion impacts the line emission.

(iv) When the wrapping radius is relatively small, the profile shape tends to deviate *less* from a flat-topped appearance, for most viewing inclinations.

(v) The compressed layer leads to line emission being sensitive to the outer spiral shape even when the wrapping radius is somewhat large.

The last point is interesting, and highlighted in Fig. 5 which also provides a test of our code for general orbits against the semi-analytic case of a conical bow shock. The figure is organized in four columns. From bottom to top, the viewing inclination ranges from pole-on to edge-on through angles of $i = 0$, 2, 10, 30, 45, 60, 80, 88 and 90°. From left- to right-hand side for the first three columns, the orbital period is 1, 100 and 10 000 yr. Profiles in the far right column are for the purely conical CWIR described in the previous section. The orbits are taken as circular, with $r_{\rm orb} = 0.001 r_{\rm c}$ so that the CWIR exists essentially everywhere. The profile shapes have not been Gaussian smoothed. The bow shock has $\beta = 40^\circ$ and the compressed layer has $\beta' = 45^\circ$ in each instance. Note that the vertical scales (not shown) are the same within a row but vary between rows.

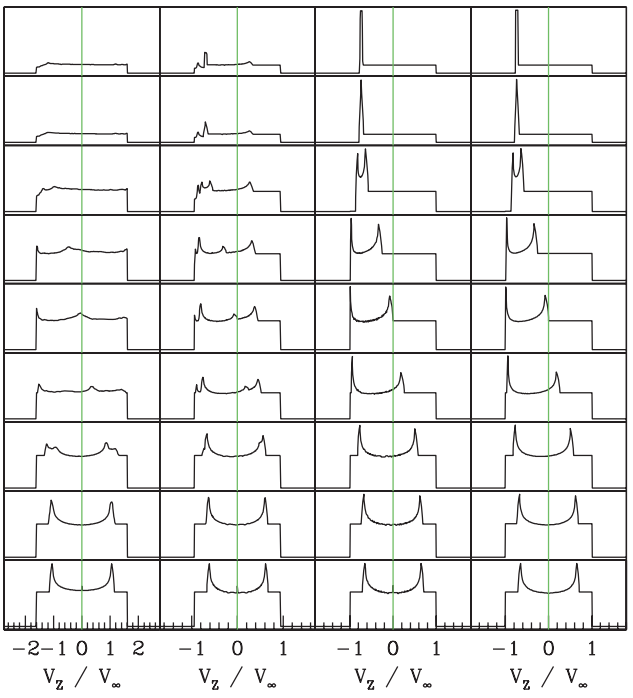

Figure 5. Shown are a series of model calculations to illustrate the range of profile shapes that result as a function of bow shock parameters, viewing perspective, and orbital parameters. The first three columns are for orbital periods of 1, 100 and 10 000 yr, respectively. The fourth column is for a strictly conical bow shock (essentially an infinite orbital period, as in Fig. 3). From top to bottom panels, the viewing inclination is $i = 0^\circ$, 2°, 10°, 30°, 45°, 60°, 80°, 88° and 90°. The orbits are circular ($e = 0$). Notably, the profile shape is sensitive to the spiral structure, a reflection of the orbital motion, even for rather long orbital periods of a century; the effectively conical bow shock limit is not achieved until a period of about 10 millennia.

For the longest period case, the profiles in the third column match those of the strict conical bow shock case in the fourth column. What is surprising is that models with $P = 100$ yr for which the wrapping radius is larger than the critical radius by two orders of magnitude deviate from the expectations of the conical bow shock case. The reason is that the emission in the compressed zone is very large. The factor of 4 increase in density combined with the density square emissivity dependence in the outer wind along with the narrowness of the zone leads to relatively 'spikey' features in velocity that appear in the line profile. Of course with instrumental smearing, the significance of these features will be substantially reduced. Also note that since the geometry is fixed, all the profiles should have the same flux, which we have confirmed.

It is clear that diverse profiles can result. Even for the highly controlled examples of Fig. 5, and with some instrumental smoothing, profiles can be largely symmetric or strikingly not so; they may have two peaks, three peaks or possibly four; and some profiles can be nearly flat-topped in shape, or have flat-toped segments.

It is difficult to explore the parameter space exhaustively owing to the large number of free parameters, namely $i, \beta, r_{\rm c}/a, r_{\rm c}/r_{\rm w}, \varphi_{\rm p}$ and φ_* plus the orbit direction, so a limited selection of illustrative results is shown in Fig. 6. These have been convolved with a Gaussian of HWHM $\delta v/v_\infty = 0.1$. Each panel is labelled. The two longer panels at right-hand side are for pole-on and edge-on viewing inclinations in which the semimajor axis takes values of $a/r_{\rm c} = 0.01$, 0.1, 1.0, five profiles for each case from bottom to top. The orbits are circular, and there are five opening angles $\beta = 30^\circ$, 40°, 50°, 60° and 70°. The orbital period is 1 yr γ Vel.

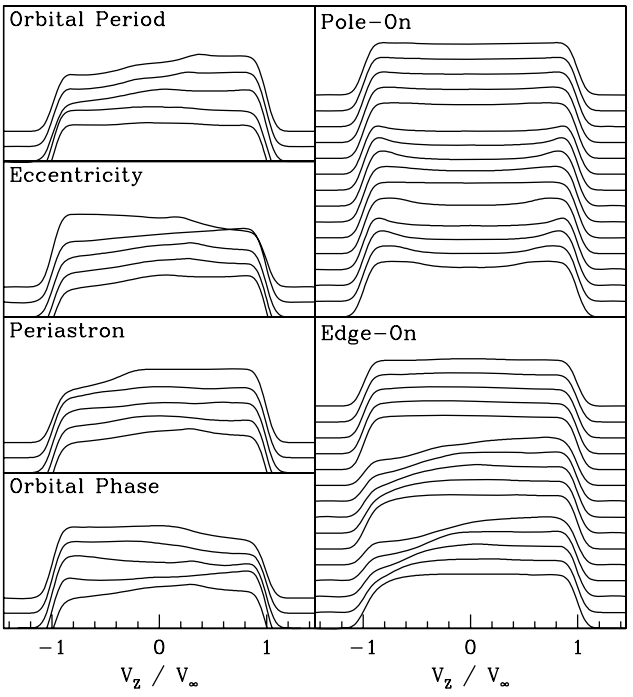

Figure 6. A selection of profile shapes as various individual orbital parameters are varied. Labels indicate control parameters. Each profile is plotted against normalized velocity shift, as in previous figures. Profiles are vertically offset for better display of profile shape effects. Specific parameter values are described in the text.

Downloaded from http://mnras.oxfordjournals.org/ at James H. Quillen College of Medicine Library on October 5, 2015

The four panels at left-hand side are for more restricted variations in the parameters as listed. Generally, $P = 1$ yr, $a/r_c = 0.1$, $e = 0.1$, $i = 60^\circ$, $\beta = 40^\circ$, and the periastron and companion star are both located at $\varphi_p = \varphi_s = 0$ for these models. The top panel shows variations in P from 0.01 to 100 yr in factors of 10 from bottom top. For eccentricity, $e = 0, 0.05, 0.1, 0.3, 0.8$, again from bottom to top. The periastron location varies from 0° to 160° in 40° increments; the same variation is used for the location of the star. Note that relative to a spherical wind, the line fluxes are never in excess by more than 23 per cent for this set of models, with an average excess of about 7 per cent.

3 DISCUSSION

There are currently relatively few WR colliding wind systems that have adequate data quality for the application of our model to interpret the CWIR geometries. *ISO* has a spectral resolving power of about 3000 but observed relatively few WR stars, and except for the fastest WR winds, the spectral resolving power of *Spitzer* is too low to resolve the features that our model predicts. However, *ISO* did observe some colliding wind binaries in its highest resolution mode, and we use two of them as test case studies: WR 147 and γ Vel (WR 11). The first is a wide binary with an unknown period, although it is likely of the order of millennia, and the second is a relatively close binary with an orbital period of a few months.

3.1 Application to WR 147

Adopted parameters for the WR 147 system are provided in Table 3. The separation of stellar components is at least 360 au, or about 10^{15} cm, based on their projected separation in the sky (Churchwell et al. 1992). The period is estimated to be at least $P \sim 10^3$ yr. The wrapping radius is thus about $\gtrsim 10^{17}$ cm. The wind density scale is around $n_{0,e} \sim 10^{11}$ cm^{-3}. We assume a statistically likely viewing inclination of 65°, in which case the orbital separation becomes 870 au. Having no other knowledge about the orbit, we adopt $e = 0$. Radio observations by Williams et al. (1997) show that the bow shock head is quite close to the companion star, for which they argue for a BV companion. The ratio of wind momenta is then $\epsilon \approx 1/90$. Using equation (22) for the bow shock opening angle for an adiabatic shock, we obtain $\beta \approx 40^\circ$.

Table 3. Wind and binary parameters for WR 147.

WR 147[a]	WN8+BV
$\dot{M}$	25×10^{-6} M$_\odot$ yr^{-1}
v_∞	950 km s^{-1}
R_*	21 R$_\odot$
μ_e	3.1
D_{cl}	10
$n_{0,e}$	1.2×10^{11} cm^{-3}
ϵ	1/90
Orbit[b]	
d	630 pc
P	1000 yr
a	870 au
e	0
i	65°
Interaction region	
β[c]	40°
r_w	330,000 R_* rad$^\circ$
r_w/r_c (Ca IV)	3300
r_w/r_c (Ne III)	330
r_w/r_c (S IV)	220

[a] Morris et al. (2000).
[b] Churchwell et al. (1992); orbital parameters are highly uncertain, but given the distance and apparent separation of the two stars, $a \sim 370/\cos i$ au.
[c] Using Gayley et al. (in preparation).

Lines of [Ca IV], [Ne III] and [S IV] were observed with *ISO* (fig. 8 of Morris et al. 2000). The WR wind density at the distance of the B star is $n_e \approx 10^3$ cm^{-3}, well beyond the critical radii values for these three lines. Deviations in the emission lines from flat-top should be mild, consistent with the observations of Morris et al. With the sulphur line forming farthest out, we might expect that some structure would be observed in it. In addition, the stellar components are separated by about $10^4 R_*$, whereas the winding radius is around 30 (or more) times that value, thus the CWIR is closely approximated by the conical bow shock model described in Section 2.4.

Synthetic spectral profiles are displayed in Fig. 7. Each panel shows model profiles plotted against normalized Doppler shift. The different profiles are for different orbital phase location, sampling a full orbit in 30° intervals. The model profiles have been convolved with a Gaussian of $\Delta v/v_\infty = 0.2$ to simulate *ISO*'s spectral resolution for the relatively lower v_∞ wind of WR 147. The line of [Ca IV] has the smallest critical radius and shows an essentially flat-toped shape. The neon and sulphur lines show greater variation, as their critical radii are somewhat closer to the B star companion. The observations of Morris et al. (2000) are suggestive of a double-horned feature in [Ne III] and [S IV], and indeed our models manage to produce such a profile shape in narrow ranges of orbital phase. However, it is unclear to what extent the profile shapes may be trusted. A re-analysis of the [Ca IV] line by Ignace et al. (2001) suggests an asymmetric line shape. If real that could indicate an

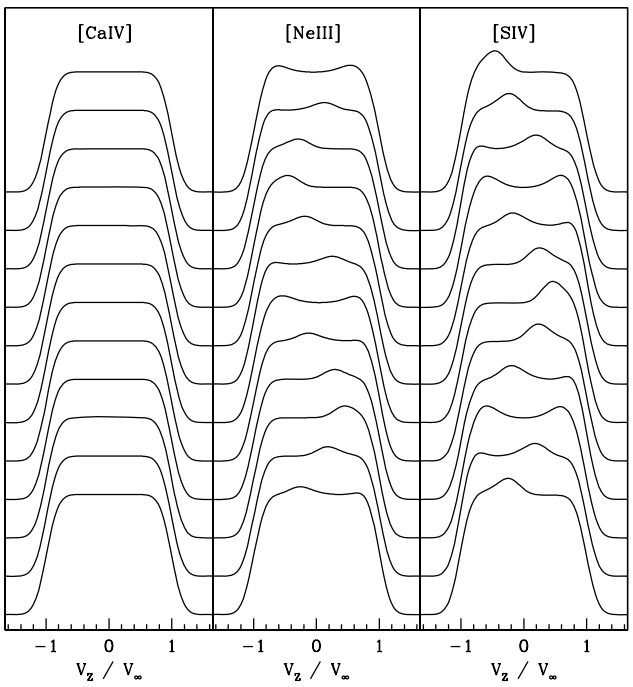

Figure 7. Model line profile shapes as indicated with application to WR 147. Each profile in a column is for a different orbital phase location of the B star companion.

Downloaded from http://mnras.oxfordjournals.org/ at James H. Quillen College of Medicine Library on October 5, 2015

elliptical orbit. A series of model runs with large eccentricities greater than 0.9 retains double-peaked morphologies in the Ne and S lines and shows some small deviations from flat-top in the Ca line for a range of orbital phases. Although better signal-to-noise ratio data at high spectral resolution is needed to measure the line shapes more accurately, this preliminary application shows intriguing potential.

3.2 Application to γ Velorum (WR 11)

Here, we apply our synthetic line profile approach to the case of γ Vel consisting of a WC8 star with an O7.5 companion. Adopted parameters for the WR wind and the orbit are given in Table 4. This colliding wind system has been studied extensively. The star and wind parameters come from de Marco et al. (2000), and the orbital parameters come from the interferometric study by North et al. (2007). Four forbidden lines were observed with *ISO*: [Ca IV], [Ne II], [Ne III] and [S IV] (see Dessart et al. 2000 and Ignace et al. 2001). In contrast to WR 147, the orbital parameters are quite well known, and so γ Vel constitutes a significant test case for our modelling. We note that the adopted opening angle of $\beta = 85^\circ$ is significantly larger than the value for an adiabatic shock at $\approx 45^\circ$ (see equation 22) or a radiative shock at $\approx 35^\circ$ (see Canto et al. 1996). We use this larger value based on the X-ray study by Henley, Stevens & Pittard (2005).

There are a number of new issues that arise in the case of γ Vel that are different from the wide binary WR 147, notably that (i) the winding radius is comparable to the critical radii of the observed forbidden lines and (ii) the critical radii of most lines are only somewhat larger than the orbital semimajor (within a factor of about 10) and for [Ca IV], the critical radius is nearly equal to the separation of the stars at apastron. The three primary scalelengths of the problem – $r_{\rm w}$, $r_{\rm orb}$ and $r_{\rm c}$ – are somewhat comparable for all four lines of interest. As a result, the single greatest deficiency of our model becomes potentially important, namely the treatment of the bow shock head.

Table 4. Wind and binary parameters for γ Vel.

WR 11[a] = γ Vel	WC8+O7.5
$\dot{M}$	$9 \times 10^{-6}\,{\rm M}_\odot\,{\rm yr}^{-1}$
v_∞	1550 km s^{-1}
R_*	3.2 R$_\odot$
$\mu_{\rm e}$	4.5
$D_{\rm cl}$	10
$n_{0,{\rm e}}$	7.8×10^{11} cm^{-3}
ϵ	1/33
Orbit[b]	
d	336 pc
P	78.53 d
a	1.2 au
e	0.334
i	65°.5
Interaction region	
φ_*^c	0.28
β^d	85°
$r_{\rm w}$	750 R_* rad°
$r_{\rm w}/r_{\rm c}$ (Ca IV)	4.2
$r_{\rm w}/r_{\rm c}$ (Ne II)	0.68
$r_{\rm w}/r_{\rm c}$ (Ne III)	0.36
$r_{\rm w}/r_{\rm c}$ (S IV)	0.13

[a] de Marco et al. (2000).
[b] North et al. (2007).
[c] $T_0 = 50120.4$ MJD and *ISO* data of γ Vel were obtained on $T = 50\,220.9836$ MJD, hence the O star was at orbital phase 0.28.
[d] Henley et al. (2005).

Our treatment of the shape of the bow shock interior to the instantaneous position of the companion star is extremely rough. We determine the stagnation point r_0 based on equation (21). The emissivity 'cavity' extends inwards in a conical fashion from the companion star to the stagnation point. This is a gross misrepresentation of the rounded shape that the bow shock should take. However, this sector of the bow shock is the portion where the two winds intersect most nearly head-on and which produces the observed X-ray emissions (e.g. Skinner et al. 2001; Henley et al. 2005). This means that the low-ionization states of calcium, neon and sulphur that contribute to the IR forbidden line emissions simply will not exist in this sector at all.

Fig. 8, left-hand side, shows synthetic emission profiles for all four observed lines in a format similar to Fig. 7 for WR 147. The model lines were Gaussian smoothed with $\Delta v/v_\infty = 0.14$ to simulate the resolution of *ISO* for the terminal speed of γ Vel's wind. The profiles are only moderately successful in reproducing the observations. Dessart et al. found that [S IV] was relatively flat-topped in appearance, whereas the neon lines produce relatively symmetric and triple-peaked profile shapes. Ignace et al. found that the calcium line was quite asymmetric, with a strong blueshifted peak. It is possible to reproduce the gross profile morphologies for calcium and sulphur, but nothing like a triple-horned shape results for the neon lines at any phase.

In order to match the profile shapes of the neon lines, an additional dependence on radius or direction is required. Although our treatment of the bow shock head is very approximate, its shortcomings are not likely to suppress a three-horned morphology. Wolf-Rainer Hamann (private communication) indicates that in the Potsdam models of WR winds, the ionization balance is still not 'frozen-in' for WC models even out to the edge of their computational grid at $200R_*$. An example of this can be seen in fig. 7 of Gräfener, Koesterke & Hamann (2002) where at the lowest wind densities in the model, ion fractions are still changing with radius. We thus choose to introduce an additional scaling parameter associated with varying ionization as given by

$$Q(r) \propto (n_{\rm e}/n_{0,{\rm e}})^p, \tag{34}$$

for some constant exponent p. Given that $n_{\rm e} \propto r^{-2}$, then $Q \propto r^{-2p}$.

The right-hand side of Fig. 8 shows model profiles with $p = 2$ for Ca^{3+}, 1 for Ne^{2+}, 2 for Ne^{1+} and 0 for S^{3+}. Note that changing p to increasingly positive values tends to move the line formation deeper into the wind, because the line luminosity scales as

$$L_v \propto \int j_v(r, \vartheta)\, Q(r)\, {\rm d}V. \tag{35}$$

In addition, the larger density in the compressed layer, by a factor of 4, tends to enhance recombination, and so for our models, we allow $p \rightarrow {\rm p} + 1$ in the shocked layer. Comparisons to detailed radiative transfer calculations, such as those of the Potsdam group or CMFGEN (Hillier & Miller 1999), are needed to assess the plausibility of the selected p values. Although motivated by the ionization considerations, $Q(r)$ mainly acts as an additional weighting function to shift the predominant region of line formation in radius.

Ultimately, our profile modelling still falls short of accurately reproducing the observed emission lines. The [Ca IV] line does become more extreme in its lopsided appearance for some phases.

Downloaded from http://mnras.oxfordjournals.org/ at James H. Quillen College of Medicine Library on October 5, 2015

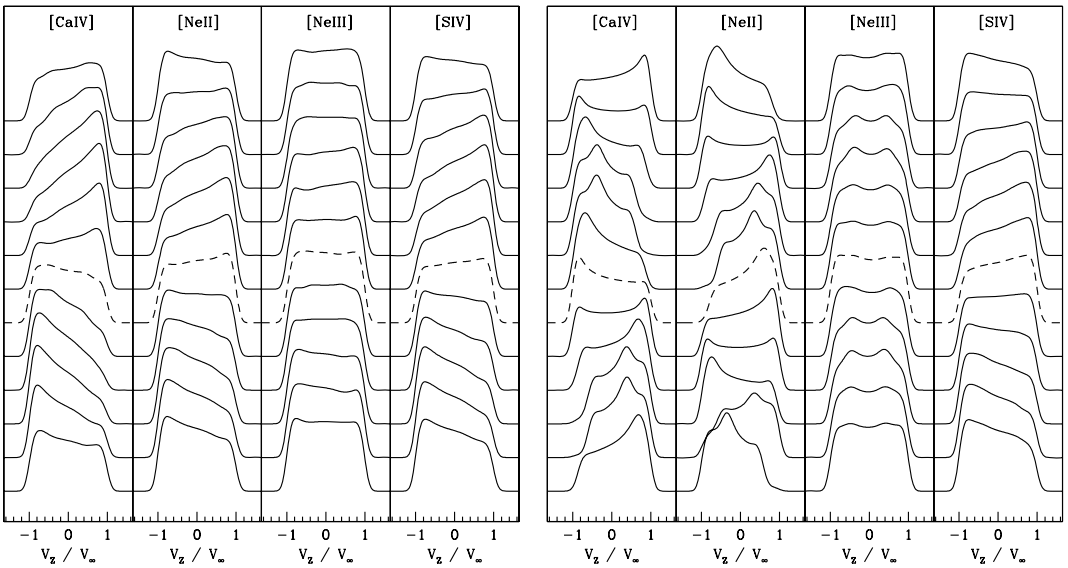

Figure 8. Similar to Fig. 7 except with application to the shorter period binary WR 11. The set of profiles at left assumes a constant ionization factor $Q(r) = Q_0$; the set at right allows for non-constant $Q(r)$ that best reflects the observed profile shapes (see the text for details). The dashed line corresponds to an orbital phase of 150°, the model closest to 143° as determined for the time that the *ISO* data were obtained.

The [Ne II] line can have a triple-horned appearance at some phases, which is a good sign; unfortunately, the triple-peaks are never as equal looking in appearance as observed. With Q a constant, the sulphur line continues to display mildly sloped or a mainly flat-topped appearance for restricted phases.

There are two main problems with the modelling for γ Vel. First, [Ne III] always shows a more or less double-horned morphology, never triple-horned as observed. Secondly, using the ephemeris of North et al. (2007), we have determined the orbital phase of γ Vel for the *ISO* line data. Note that an independent study by Millour et al. (2007) yields mostly similar parameters. According to North et al., the O star orbits counterclockwise on the sky, and so the CWIR spirals outwards in a clockwise fashion. According to the *ISO* archive, the data were obtained on 1996 May 17 at 23:36:24, or MJD 50220.9836. Using the observation of North et al. on MJD 50120.4 and a period of $P = 78.53$ d, the O star is 28 per cent of an orbit past periastron in time, which corresponds to an orbital phase of 143°. In our simulations, this is close to a phase of 150° that is plotted as a dashed line. Thus, the second problem is that we cannot simultaneously get all four profiles with the overall grossly correct morphologies at quite the same phase. Note that at a nearby phase of 120°, the [Ne II] line does show a triple peak.

4 CONCLUSION

Our study concerns model calculations for forbidden emission-line profile shapes that form in a colliding wind system. The approach recognizes that spherically symmetric winds produce optically thin and flat-topped emission-line shapes produced in the constant expansion flow. Deviations from that flat-toped morphology represent an opportunity to infer information about the orbital properties of the binary and the colliding wind bow shock.

Our approach makes a number of significant simplifications to make the problem tractable: the OB companion wind makes no contribution to the line emission, flow in the compressed layer is radial and with the same speed as the WR wind, the extent of the shocked layer is only approximate, the geometry of the bow shock head is treated poorly, the bow shock is assumed axisymmetric about the line of centres for the two stars and more input regarding the ionization balance in the large-scale wind is needed to model line shapes properly.

In light of all of these shortcomings, the models do produce a remarkable degree of diverse profile morphologies. Although even qualitative matches to observed forbidden lines from WR 147 and γ Vel are far from satisfactory, the attempt does appear to capture a number of trends and shows potential as a tool for deducing or limiting orbital and wind parameters.

Although of lower spectral resolution than *ISO*, we determined that the *Spitzer* IRS could probably detect modulations of IR forbidden line shapes with orbital phase. Unfortunately, the IRS will not be available during *Spitzer's* 'warm' cycle. It is expected that the James Webb Space Telescope will have a mid-IR spectrograph[1] with a resolving power similar to *ISO*. In addition, the [Ne II] emission line is observable from ground-based observatories, as for example in the study of Smith & Houck (2001). In particular, their sample included WR 146 which has quite broad lines owing to a wind terminal speed of nearly 3000 km s^{-1}. So there is the possibility that future observations will provide new high-quality data of these and other systems for which our diagnostics will be relevant.

ACKNOWLEDGMENTS

We wish to thank Ken Gayley for helpful discussions in the early stages of this project. We are also grateful a number of useful suggestions made by an anonymous referee. This project was funded by a partnership between the National Science Foundation (NSF AST-0552798), Research Experiences for Undergraduates (REU) and the Department of Defense (DoD) ASSURE (Awards to Stimulate and Support Undergraduate Research Experiences) programmes.

REFERENCES

Antokhin I. I., Owocki S. P., Brown J. C., 2004, ApJ, 611, 434
Barlow M. J., Roche P. F., Aitken D. K., 1988, MNRAS, 232, 821

[1] www.stsci.edu/jwst/instruments/miri

© 2009 The Authors. Journal compilation © 2009 RAS, MNRAS **395,** 962–972

Downloaded from http://mnras.oxfordjournals.org/ at James H. Quillen College of Medicine Library on October 5, 2015

Brown J. C., McLean I. S., Emslie A. G., 1978, A&A, 68, 415
Canto J., Raga A. C., Wilkin F. P., 1996, ApJ, 469, 729
Cassinelli J. P., Ignace R., Waldron W. L., Cho J., Murphy N. A., Lazarian A., 2008, ApJ, 683, 1052
Churchwell E., Bieging J. H., van der Hucht K. A., Williams P. M., Spoelstra T. A., Abbott D. C., 1992, ApJ, 393, 329
de Graauw T. et al., 1996, A&A, 315, L49
de Marco O., Schmutz W., Crowther P. A., Hillier D. J., Dessart L., de Koter A., Schweickhardt J., 2000, A&A, 358, 187
Dessart L., Crowther P. A., Hillier D., Willis A. J., Morris P. W., van der Hucht K. A., 2000, MNRAS, 315, 407
Drissen L., Moffat A. F. J., Bastien P., Lamontagne R., Tapia S., 1986, ApJ, 306, 215
Gayley K. G., Owocki S. P., Cranmer S. R., 1997, ApJ, 131, 237
Girard T., Willson L. A., 1987, A&A, 183, 246
Gräfener G., Koesterke L., Hamann W.-R., 2002, A&A, 387, 244
Henley D. B., Stevens I. R., Pittard J. M., 2003, MNRAS, 346, 773
Henley D. B., Stevens I. R., Pittard J. M., 2005, MNRAS, 356, 1308
Hill G. M., Moffat A. F. J., St-Louis N., Bartzakos P., 2000, MNRAS, 318, 402
Hill G. M., Moffat A. F. J., St-Louis N., 2002, MNRAS, 335, 1069
Hillier D. J., Miller D. L., 1999, ApJ, 519, 354
Ignace R., Brimeyer A., 2006, MNRAS, 371, 343
Ignace R., Cassinelli J. P., Quigley M., Babler B., 2001, ApJ, 558, 771
Ignace R., Cassinelli J. P., Tracy G., Churchwell E. B., Lamers H. J. G. L. M., 2007, ApJ, 669, 600
Lamers H. J. G. L. M., Cassinelli J. P., 1999, Introduction to Stellar Winds. Cambridge Univ. Press, New York
Lührs S., 1997, PASP, 109, 504
Maeda Y., Koyama K., Yokogawa J., Skinner S., 1999, ApJ, 510, 967
Millour F. et al., 2007, A&A, 464, 107
Monnier J. D., Tuthill P. G., Danchi W. C., 1999, ApJ, 525, L97
Monnier J. D., Greenhill L. J., Tuthill P. G., Danchi W. C., 2002, ApJ, 566, 399
Morris P. W., van der Hucht K. A., Crowther P. A., Hillier D. J., Dessart L., Williams P. M., Willis A. J., 2000, A&A, 353, 624
Morris P. W., Crowther P. A., Houck J. R., 2004, ApJS, 154, 413
North J. R., Tuthill P. G., Tango W. J., Davis J., 2007, MNRAS, 377, 415
Osterbrock D. E., 1989, Astrophysics of Gaseous Nebulae and Active Galactic Nuclei. University Science Books, Mill Valley
Parkin E. R., Pittard J. M., 2008, MNRAS, 388, 1047
Pittard J. M., Stevens I. R., Williams P. M., Pollock A. M. T., Skinner S. L., Corcoran M. F., Moffat A. F. J., 2002, A&A, 388, 335
Pradhan A. K., Peng J., 1995, in Williams R. E., Livio M., eds, Analysis of Emission Lines. Cambridge Univ. Press, Cambridge, p. 8
Smith J.-D. T., Houck J. R., 2001, AJ, 121, 2115
Smith J.-D. T., Houck J. R., 2005, ApJ, 622, 1044
Shore S. N., Brown D. N., 1988, ApJ, 334, 1021
Skinner S. L., Güdel M., Schmutz W., Stevens, I. R., 2001, ApJ, 558, L113
Stevens I. R., 1993, ApJ, 404, 281
Stevens I. R., Howarth I. D., 1999, MNRAS, 302, 549
Stevens I. R., Blondin J. M., Pollock A. M. T., 1992, ApJ, 386, 265
Stevens I. R., Corcoran M. F., Willis A. J., Skinner S. L., Pollock A. M. T., Nagase F., Koyaman K., 1996, MNRAS, 283, 589
Tuthill P. G., Monnier J. D., Danchi W. C., 1999, Nat, 398, 487
Tuthill P. G., Monnier J., Tanner A., Figer D., Ghez A., Danchi W., 2006, Sci, 313, 935
Tuthill P. G., Monnier J. D., Lawrance N., Danchi Wi. C., Owocki S. P., Gayley K. G., 2008, ApJ, 675, 698
Usov V. V., 1992, ApJ, 389, 635
Villar-Sbaffi A., Moffat A. F. J., St-Louis N., 2003, ApJ, 590, 483
Villar-Sbaffi A., St-Louis N., Moffat A. F. J., Piirola V., 2005, ApJ, 623, 1092
Villar-Sbaffi A., St-Louis N., Moffat A. F. J., Piirola V., 2006, ApJ, 640, 995
Williams P. M., Dougherty S. M., Davis R. J., van der Hucht K. A., Bode M. F., Setia Gunawan D. Y. A., 1997, MNRAS, 289, 10
Willis A. J., Dessart L., Crowther P. A., Morris P. W., Maeder, A., Conti P. S., van der Hucht K. A., 1997, MNRAS, 290, 371
Zhekov S. A., Skinner S. L., 2000, ApJ, 538, 808

This paper has been typeset from a TEX/LATEX file prepared by the author.

Downloaded from http://mnras.oxfordjournals.org/ at James H. Quillen College of Medicine Library on October 5, 2015